Current Applied Physics 14 (2014) 1794–1802

Contents lists available at ScienceDirect

Current Applied Physics

journal homepage: www.elsevier.com/locate/cap

Development of lattice inversion modified embedded atom method and its applications

Xianbao Duan [a], Bing Zhou [b], Rong Chen [b], Huamin Zhou [a], Yanwei Wen [a, **], Bin Shan [a, c, *]

[a] State Key Laboratory of Materials Processing and Die and Mould Technology and School of Materials Science and Engineering, Huazhong University of Science and Technology, Wuhan 430074, Hubei, People's Republic of China
[b] State Key Laboratory of Digital Manufacturing Equipment and Technology and School of Mechanical Science and Engineering, Huazhong University of Science and Technology, Wuhan 430074, Hubei, People's Republic of China
[c] Department of Materials Science and Engineering, The University of Texas at Dallas, Richardson, TX 75080, USA

ARTICLE INFO

Article history:
Received 2 July 2014
Received in revised form
20 October 2014
Accepted 20 October 2014
Available online 27 October 2014

Keywords:
MEAM
Lattice inversion
Interatomic potential
Molecular dynamics

ABSTRACT

The modified embedded atom method (MEAM) has been widely used in describing the physical properties of elemental crystals, alloys and compounds with multiple lattice structures. We report here the development of a reliable procedure to reduce the complexity of the MEAM formalism by removing the many-body screening function. In the proposed formulation, the interatomic pair potential is obtained by applying Chen-Möbius lattice inversion up to fifth nearest neighbors, so that the cohesive energy curve can be reproduced faithfully. The newly developed model (Lattice Inversion MEAM, LI-MEAM), which can be viewed as a direct extension of the embedded atom method (EAM), no longer requires the computation of many-body screen functions and has fewer adjustable parameters than MEAM. As an illustration, we optimized the potential parameters of body centered cubic iron (bcc-Fe). The values of the calculated physical properties agree well with experimental results. We further investigated the size-dependent melting behavior of bcc-Fe nanoparticles (NPs) with particle size ranging from 725-atom (~25 Å) to 22899-atom (~80 Å) using replica exchange molecular dynamics (REMD) simulations. Our simulations show advantages of LI-MEAM in modeling of the melting process and quantitatively reveals that the liquid skin melting (LSM) process of bcc-Fe NPs.

1. Introduction

Atomistic simulations are powerful techniques to explore the physical properties of materials on micro scales. While simulations with billions of atoms or millisecond time span can be achieved on super computers nowadays [1,2], the reliability and accuracy of the simulation results depend critically on the quality of the interatomic potentials [3]. Many efforts have been devoted to the development of more accurate and reliable potentials for describing the interactions between specific atoms [4–8]. Among the various models, the embedded atom method (EAM) proposed by Daw et al. [4,5] is an elegant and powerful model for describing atomic interactions in bulk metals. To make EAM applicable to more complex systems, several modifications and extensions to EAM were proposed. Johnson and Oh [9,10] developed the analytical embedded atom method by choosing appropriate analytical forms for all the EAM functions (AEAM). Later on, Zhang, Hu and Ouyang [11,12] added an analytical modification term to the AEAM expression of cohesive energy and proposed a modified form of the EAM potential. Lee and Cho [13] extended EAM by introducing a local structural dependent prefactor with three additional parameters to account for the bond characteristics arising from asymmetrical surface atoms. Shan et al. [14] reported an extension of EAM potentials applied to alloy nanoparticles by refining the original EAM embedding and cross-pair functionals. Some works have also been done to improve the EAM accuracy by incorporating the Chen-Möbius lattice inversion [15–19] method into the potential fitting process [20–23]. In summary, most of these extended models could show relatively good performance in describing the properties of specific systems. However, due to the lack of angular electron density dependence, EAM derived models in general lack the transferability to apply to other none-close packed structures,

* Corresponding author. State Key Laboratory of Materials Processing and Die and Mould Technology and School of Materials Science and Engineering, Huazhong University of Science and Technology, Wuhan 430074, Hubei, People's Republic of China.
** Corresponding author.
E-mail addresses: ywwen@hust.edu.cn (Y. Wen), bshan@mail.hust.edu.cn (B. Shan).

http://dx.doi.org/10.1016/j.cap.2014.10.014
1567-1739/

complex oxides, or systems with partial covalent bonding characteristics [3].

Aimed at improving the description of directional bonding in solids, Baskes et al. [24–27] modified the EAM by considering three directional partial electron densities in addition to the original spherical component, which conceptually represent p, d, f orbitals with different angular momentum, and put forward the modified embedded atom method (MEAM). Due to the consideration of the interactions from only the first nearest neighbors, it is also named as the first nearest-neighbor MEAM (1NN MEAM). The 1NN MEAM stands out for its universality and accuracy, and could describe the properties of a variety of metals and alloys accurately [26,27]. However, it faces difficulties in modeling some bcc transition metals, such as incorrect ordering among low-index surface energies and structural instability [28]. In order to mitigate these shortcomings, Lee et al. [28] modified 1NN MEAM by extending the interactions to the second nearest neighbors, and proposed the second nearest-neighbor MEAM (2NN MEAM). Compared to 1NN MEAM and previous EAM models, 2NN MEAM is a more accurate model for describing metals, alloys and covalent systems. Much efforts have also been made by Lee et al. [28–31] and other researchers [32,33] on building up a database of potential parameters based on 2NN MEAM.

In the practical application of MEAM (If not specified below, MEAM refers to both 1NN MEAM and 2NN MEAM.), an additional many-body screening function must be introduced to cutoff the interactions from neighbors beyond first or second nearest neighbors on the electron densities and pair energies, which increases the complexity of this model [26–28]. Furthermore, there seems to be a lack of systematic way for the determination of the parameters associated with the many-body screening function. For pure element, there are two parameters, $C_{\max}$ and $C_{\min}$, which are related to screening function. But the parameter set quickly grow into a large set as a total of eight parameters of $C_{\max}$ and $C_{\min}$ (A-A-B, B-B-A, A-B-A, A-B-B) are needed for binary AB alloys, and the parameter size increase exponentially for multicomponent systems [3,31,33]. In MEAM formalism where the interaction is limited to first or second neighbors, the many-body screening function is needed as a practical approach to obtain the desired accuracy. In the present work, we report the reformulation of the MEAM model by using Chen-Möbius lattice inversion method (Lattice Inversion MEAM, LI-MEAM). By incorporating the lattice inversion technique, we have successfully removed the many-body screening function, which makes MEAM formalism simpler. From another point of view, it provides transparent physics, which can be viewed as a direct extension of EAM by considering the directional partial electron densities. Also, the number of adjustable parameters has been reduced. In order to validate the developed LI-MEAM model, the potential was parameterized for body centered cubic iron (bcc-Fe), which is a classical benchmark for many body potentials. Some key physical properties of Fe were calculated and compared with the results of experiments and other potential models. Furthermore, the size-dependent melting behavior of bcc-Fe nanoparticles (NPs) was investigated using replica exchange molecular dynamics (REMD) simulations [34,35].

2. Methodology

2.1. Chen-Möbius lattice inversion

Chen-Möbius inversion formula was first derived by Chen based on the number theory [15] and then applied to a variety of inverse problems in physics [36–38]. Later on, Chen et al. [17–19] developed a series of lattice inversion methods by inverting cohesion for interatomic potential in bulk materials and adhesion for interatomic potential across interfaces. The following is a brief introduction to the fundamentals of Chen-Möbius lattice inversion.

Theoretically speaking, any cohesive energy for a multidimensional crystal lattice can be expressed as a sum of many-body interactions, which include two-body, three-body, …, n-body interactions. If only two-body interactions are considered, the expression for cohesive energy per atom, E, can be simplified as the following:

$$E = \frac{1}{2}\sum_{j(\neq i)} \Phi(r_{ij}), \tag{1}$$

where r_{ij} represents the lattice vector from site i to site j, $\Phi(r_{ij})$ is the corresponding pair potential. Considering a standard reference structure, such as bcc or fcc, $\Phi(r_{ij})$ can be expanded along the orders of nearest neighbors, then Eq. (1) can be written as:

$$E(r) = \frac{1}{2}\sum_{m=1}^{\infty} Z_0^{(m)} \Phi\left(a_0^{(m)} r\right), \tag{2}$$

where m is the order of the nearest neighbors and ranges from 1 to infinity, $Z_0^{(m)}$ is the actual number of m-th nearest neighbors, $a_0^{(m)}$ is the ratio of the distance of m-th nearest neighbors to r, which is the distance for the first nearest neighbors.

In order to apply Chen-Möbius lattice inversion to obtain pair potential function from Eq. (2), a mathematic technique is used to extend the original series $\{a_0^{(m)}\}$ to a multiplicative semi-group $\{a^{(m)}\}$ such that, for any two integers i and j, an integer k always exists which satisfying:

$$a^{(i)}a^{(j)} = a^{(k)}. \tag{3}$$

Then Eq. (2) can be rewritten as:

$$E(r) = \frac{1}{2}\sum_{m=1}^{\infty} Z^{(m)} \Phi\left(a^{(m)} r\right), \tag{4}$$

where

$$Z^{(m)} = \begin{cases} Z_0\left(a_0^{-1}\left[a^{(m)}\right]\right) & a^{(m)} \in \left\{a_0^{(m)}\right\} \\ 0 & a^{(m)} \notin \left\{a_0^{(m)}\right\} \end{cases}. \tag{5}$$

Note that $\{Z_0^{(m)}\}$ is the actual numbers of the m-th nearest neighbors, and $\{Z^{(m)}\}$ is the extended group which contains $\{Z_0^{(m)}\}$ with all the additive elements equal to zeros. Eq. (4) is a standard form available for applying Chen-Möbius lattice inversion directly to invert the relationship between the two involved functions, saying $E(r)$ and $\Phi(r)$. The inverted equation is shown as:

$$\Phi(r) = 2\sum_{m=1}^{\infty} I^{(m)} E\left(a^{(m)} r\right), \tag{6}$$

where the inversion coefficient $I^{(m)}$ is given by:

$$\sum_{a^{(m)}|a^{(k)}} I^{(m)} Z\left[a^{-1}\left(\frac{a^{(k)}}{a^{(m)}}\right)\right] = \delta_{k1}, \tag{7}$$

and δ_{k1} is Kronecker delta function.

Fig. 1 shows the scheme about how to obtain the pair potential from the cohesive energy by applying Chen-Möbius lattice inversion. The arrows in the figure represent the determinant relationships between the involved parameters or physical quantities. In details, the cohesive energy $E(x)$ can be obtained from experiments

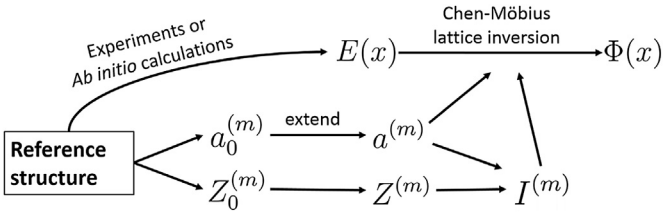

Fig. 1. Schematic diagram about how to obtain the pair potential from cohesive energy by applying Chen-Möbius lattice inversion.

or *ab initio* calculations. The involved coefficients $I^{(m)}$ and $a^{(m)}$ can be calculated from the reference structure uniquely. Then the pair potential can be yielded from Eq. (6). In practical, finite but enough items are used in Eqs. (4) and (6) to guarantee appropriate accuracy and efficiency.

2.2. Lattice inversion MEAM

Compared to previous MEAM models, the main modification of LI-MEAM lies in the removal of the many-body screening function, and the inclusion of the interactions from farther nearest neighbors by applying Chen-Möbius lattice inversion. Details of previous MEAM models can be found in Ref. [28]. In this subsection, we introduce the formulations of the developed LI-MEAM model briefly and point out the main differences.

The total energy per atom for an arbitrary system in LI-MEAM is composed of two parts, the embedding energy and the pair energy, as:

$$(E)_{\mathrm{LI-MEAM}} = F(\overline{\rho}_i) + \frac{1}{2}\sum_{i\neq j}\Phi(r_{ij}), \tag{8}$$

where F is the embedding function, $\overline{\rho}_i$ is the background electron density at site i, $\Phi(r_{ij})$ is the pair potential between atoms i and j at a distance r_{ij}. As a comparison, the corresponding equation in previous MEAM models can be given by considering the many-body screening function, S_{ij}, as:

$$(E)_{\mathrm{MEAM}} = F(\overline{\rho}_i) + \frac{1}{2}\sum_{i\neq j}\Phi(r_{ij})S_{ij}. \tag{9}$$

The embedding functions in Eq. (8) and Eq. (9) are the same and given by:

$$F(\overline{\rho}) = AE_c\left(\overline{\rho}/\overline{\rho}^0\right)\ln\left(\overline{\rho}/\overline{\rho}^0\right), \tag{10}$$

where A is the scaling factor, E_c is the sublimation energy, $\overline{\rho}^0$ is the background electron density for the reference structure. Usually, for a specified element, the equilibrium structure is taken as the reference structure. The background electron density $\overline{\rho}_i$ in Eq. (8) is given by:

$$\overline{\rho}_i = \overline{\rho}_i^{(0)}G(\Gamma), \tag{11}$$

where

$$G(\Gamma) = 2\Big/\left(1+e^{-\Gamma}\right) \tag{12}$$

and

$$\Gamma = \sum_{k=1}^{3} t_i^{(k)}\left(\frac{\overline{\rho}_i^{(k)}}{\overline{\rho}_i^{(0)}}\right)^2. \tag{13}$$

In the equations, $\overline{\rho}_i^{(k)}$ $(k = 0,1,2,3)$ represent the spherical $(k = 0)$ and angular $(k = 1,2,3)$ electron densities. $t_i^{(k)}$ $(k = 1,2,3)$ are the corresponding weighting factors for the three angular electron densities. $\overline{\rho}_i^{(k)}$ are given by:

$$\left(\overline{\rho}_i^{(0)}\right)^2 = \left[\sum_{j\neq i}\rho_j^{a(0)}\right]^2 \tag{14a}$$

$$\left(\overline{\rho}_i^{(1)}\right)^2 = \sum_{\alpha}\left[\sum_{j\neq i}\frac{r_{ij}^{\alpha}}{r_{ij}}\rho_j^{a(1)}\right]^2 \tag{14b}$$

$$\left(\overline{\rho}_i^{(2)}\right)^2 = \sum_{\alpha,\beta}\left[\sum_{j\neq i}\frac{r_{ij}^{\alpha}r_{ij}^{\beta}}{r_{ij}^2}\rho_j^{a(2)}\right]^2 - \frac{1}{3}\left[\sum_{j\neq i}\rho_j^{a(2)}\right]^2 \tag{14c}$$

$$\left(\overline{\rho}_i^{(3)}\right)^2 = \sum_{\alpha,\beta,\gamma}\left[\sum_{j\neq i}\frac{r_{ij}^{\alpha}r_{ij}^{\beta}r_{ij}^{\gamma}}{r_{ij}^3}\rho_j^{a(3)}\right]^2 - \frac{3}{5}\sum_{\alpha}\left[\sum_{j\neq i}\frac{r_{ij}^{\alpha}}{r_{ij}}\rho_j^{a(3)}\right]^2. \tag{14d}$$

Here, $\rho_j^{a(k)}$ $(k = 0,1,2,3)$ are the atomic electron densities of atom j for different directions. r_{ij}^{α}, r_{ij}^{β}, r_{ij}^{γ} are the α, β, γ components of r_{ij}, respectively. Similarly, the corresponding electron densities for previous MEAM models can be expressed by multiplying all the $\rho_j^{a(k)}$ in Eq. (14) by the same screening function, S_{ij}, as:

$$\left(\overline{\rho}_i^{(k)}\right)_{\mathrm{MEAM}} = \left(\overline{\rho}_i^{(k)}\right)_{\mathrm{LI-MEAM}}S_{ij}. \tag{15}$$

$\rho_i^{a(k)}$ in Eq. (14) and Eq. (15) have the following form:

$$\rho_i^{a(k)}(r_{ij}) = e^{-\beta_i^{(k)}\left(r_{ij}/r_e-1\right)}, \tag{16}$$

where $\beta_i^{(k)}$ $(k = 0,1,2,3)$ are decay factors for corresponding atomic electron densities, r_e is the nearest neighbor distance in the equilibrium reference structure.

The next step is to determine the pair potential $\Phi(r_{ij})$ in Eq. (8) so that the total energy for an arbitrary system can be calculated. To obtain the pair potential, a reference structure should be selected so that the total energy (or called cohesive energy) could be determined according to experimental data or *ab initio* calculations directly. Herein, the universal equation of state proposed by Rose et al. [39], is used to express the total cohesive energy per atom for the reference structure, E^u, as a function of the nearest-neighbor distance r:

$$E^u(r) = -E_c(1+a^*)e^{-a^*}, \tag{17}$$

where

$$a^* = \alpha(r/r_e - 1) \tag{18}$$

and

$$\alpha = \sqrt{9B\Omega/E_c}. \tag{19}$$

Here, B is bulk modulus. Ω is equilibrium atomic volume, which is dependent on the equilibrium nearest-neighbor distance r_e.

The pair energy per atom could thus be calculated by subtracting the embedding energy from the cohesive energy. Normally, the pair energy is expressed as the accumulation of the pair potentials of the surrounding neighbors. In practice, 1NN MEAM only accumulates the pair potentials of the first nearest neighbors, while 2NN MEAM includes the pair interactions from both the first and

the second ones. As for LI-MEAM, the pair potentials of arbitrary nearest neighbors can be considered in theory. In practical implementation, a cutoff distance r_c is introduced to consider finite but enough nearest neighbors, as:

$$E^u(r) - F\left[\bar{\rho}^0(r)\right] = \frac{1}{2}\sum_{m=1}^{a_0^m r < r_c} Z_0^{(m)}\Phi\left(a_0^{(m)} r\right), \tag{20}$$

where $Z_0^{(m)}$ and $a_0^{(m)}$ are the same as those in Eq. (2). Besides, in order to improve the performance of the cutoff effect, the smooth radial cutoff function, $f_c[(r_c - r)/\Delta r]$, which was also used in previous MEAM models, is preserved in LI-MEAM to handle on all the cutoff regions, where f_c is the smooth cutoff function given by:

$$f_c(x) = \begin{cases} 1, & x \geq 1 \\ \left[1 - (1-x)^4\right]^2, & 0 < x < 1 \\ 0, & x \leq 0 \end{cases}, \tag{21}$$

and Δr is the cutoff region. For present work, Δr was given 0.2.

In order to apply Chen-Möbius lattice inversion on Eq. (20) to obtain the pair potential, the involved series $\{Z_0^{(m)}\}$ and $\{a_0^{(m)}\}$ should be firstly extended to corresponding multiplicative semigroups $\{Z^{(m)}\}$ and $\{a^{(m)}\}$ according to the method introduced in section 2.1. Then the following equation can be obtained:

$$E^u(r) - F\left[\bar{\rho}^0(r)\right] = \frac{1}{2}\sum_{m=1}^{a^{(m)} r < r_c} Z^{(m)}\Phi\left(a^{(m)} r\right). \tag{22}$$

If the left two items in Eq. (22) are regarded as one, it is with the same form as Eq. (4). So Eq. (22) can be inverted to obtain the pair potential function by applying Chen-Möbius lattice inversion. The following equation shows the inverted function:

$$\Phi(r) = 2\sum_{m=1}^{a^{(m)} r < r_c} I^{(m)}\left\{E^u\left(a^{(m)} r\right) - F\left[\bar{\rho}^0\left(a^{(m)} r\right)\right]\right\}. \tag{23}$$

where the inversion coefficient series $\{I^{(m)}\}$ is decided by $\{Z^{(m)}\}$ and $\{a^{(m)}\}$ uniquely and can be calculated using Eq. (7). Using Eq. (23), the pair potential can be obtained, which can be used in Eq. (8) to calculate the total energy of arbitrary systems.

In summary, there are totally 12 parameters involved for one single element in LI-MEAM, as the scaling factor A, the sublimation energy E_c, the equilibrium nearest-neighbor distance r_e, the bulk modulus B, the weight factors $t_i^{(k)}$ ($k = 1,2,3$), the decay factors $\beta^{(k)}$ ($k = 0,1,2,3$) and the cutoff distance r_c. The parameters, C_{max} and C_{min}, which are used in previous MEAM models, are no longer needed for the many-body screening function.

2.3. Melting behavior of NPs using REMD

Due to the consideration of interactions from farther nearest neighbors, LI-MEAM normally uses relatively large cutoff distance, r_c, compared with previous MEAM models. Considering that the melting behavior of NPs were generally investigated by using long–range interaction potentials, such as Finnis-Sinclair potential, Sutton-Chen potential [35,40–42], it serves as a good case for testing the accuracy and reliability of the LI-MEAM model.

Melting behavior is one of the most fundamental physical properties for NPs. Many attentions have been paid to studying the relationship between the sizes of NPs and the melting points, and further discovering the melting mechanism of NPs [35,41,43–47]. Many different models have been proposed to explain the mechanism of the melting behavior of NPs [35,44–47]. Among the various models, the homogeneous melting (HGM) model and liquid skin melting (LSM) model are most widely used for the melting of spherical NPs [44]. The HSM model considers that the entire NP melts homogeneously, while LSM model considers that an outer liquid shell of constant thickness forms before the melting of the entire NP. For HGM model, the relationship between the melting point and the size of NPs can be expressed as:

$$\frac{T_{cm}}{T_{bm}} = 1 - \frac{\beta_{HGM}}{D}, \tag{24}$$

while that of LSM model can be given by:

$$\frac{T_{cm}}{T_{bm}} = 1 - \frac{\beta_{LSM}}{D - 2\delta}, \tag{25}$$

where T_{cm} and T_{bm} are the melting points of the NP and the corresponding bulk material, respectively, D is the diameter of the NP, β_{HGM} and β_{LSM} are material constants for HGM model and LSM model, respectively, δ is the thickness of the outer liquid shell in LSM model. From Eqs. (24) and (25), the melting point of NP, T_{cm}, depends linearly on the inverse diameter of NP, $1/D$, for HGM model, but non-linearly for LSM model.

The most straightforward method for the calculation of melting point is carrying out molecular dynamics (MD) simulations of a perfect lattice at increasing temperatures, which is called hysteresis method. The temperature at which the potential energy per atom increases sharply corresponds to the melting point. However, superheating or undercooling usually occurs during MD simulations, which results in an overestimation of the melting points. In order to mitigate the problem, Shu et al. applied replica exchange molecular dynamics (REMD) [34] to the determination of the melting point of NP and showed better accuracy in contrast to the conventional MD methods [35]. In present work, REMD method was adopted to calculate all the melting points, both for bulk and NPs.

In order to probe the size-dependent melting point of bcc-Fe NPs based on the developed LI-MEAM model, melting of different sizes of spherical bcc-Fe NPs with the diameters ranging from 25 Å to 80 Å (corresponding atom number, N, from 725 to 22899), were simulated by REMD. The initial structures of all the NPs were approximately spherically cut out from the bulk phase [35,44]. In all the REMD simulations, the time step for integration was 1 fs (fs), and the NVT ensemble was applied. Meanwhile, 16 temperatures were used for all the NPs and the temperatures were selected near the melting point of each NP. The total simulation time of each replica for all systems was 5 ns (ns) [35], which was proved to be sufficient for equilibration. The replicas were exchanged every 1 ps (ps). For each temperature (replica), the physical quantities were averaged within the last 2 ns. For each sweep of 2 ps, the first ps was used for the equilibrium of the system, and only the second ps was used for statistics. All the related simulations in present work were performed by using the LAMMPS code. [48].

3. Results and discussion

3.1. Determination of the parameters

As introduced in subsection 2.2, a total of 12 parameters are used in LI-MEAM model. These parameters are listed in Table 1. Among which, E_c, r_e and B were given experimentally, and $\beta^{(1)}$, $\beta^{(2)}$, $\beta^{(3)}$ were given the same values as those in previous MEAM models. Therefore, only 6 adjustable parameters were needed to be determined for single element, i.e. A, $\beta^{(0)}$, $t^{(1)}$, $t^{(2)}$, $t^{(3)}$ and r_c.

Table 1
Optimized parameters of bcc-Fe based on LI-MEAM potential, in comparison with those based on 1NN MEAM and 2NN MEAM. Values listed are the sublimation energy E_c(eV), the equilibrium nearest-neighbor distance r_e(Å), the bulk modulus B(10^{12}dyn/cm^2), the exponential decay factors for the atomic densities $\beta^{(0)}$, $\beta^{(1)}$, $\beta^{(2)}$, $\beta^{(3)}$, the scaling factor for the embedding energy A, the weighting factors for the atomic densities $t^{(1)}$, $t^{(2)}$, $t^{(3)}$, the cutoff distance r_c, and the adjustable factors for screening function $C_{\max}$ and $C_{\min}$.

	E_c	r_e	B	$\beta^{(1)}$	$\beta^{(2)}$	$\beta^{(3)}$	A	$\beta^{(0)}$	$t^{(1)}$	$t^{(2)}$	$t^{(3)}$	r_c	$C_{\max}$	$C_{\min}$
1NN MEAM	4.29	2.48	1.67	1.00	1.00	1.00	0.89	2.94	3.04	4.12	−1.50	4.0	2.80	2.00
2NN MEAM	4.29	2.48	1.67	1.00	1.00	1.00	0.57	3.67	2.90	1.00	−8.50	4.0	2.80	0.16
LI-MEAM	4.29	2.48	1.67	1.00	1.00	1.00	0.532	4.182	−0.778	8.724	5.171	5.678		

In present work, bcc-Fe was chosen as an illustration to validate LI-MEAM potential because it's a typical non-close packed system to test the availability of interatomic potential [23,28]. In order to determine the above 6 potential parameters for bcc-Fe, some physical properties, elastic constants (C_{11}, C_{44}), vacancy formation energy (E_v^f), structure energy difference between bcc and fcc ($\Delta E_{bcc\to fcc}$), surface energy of the lowest surface (110) ($E_{(110)}$), were selected as the optimization targets. C_{12} was not taken into account, since it can be determined from C_{11} and B in cubic systems. In experiment, obtaining the surface energy of each surface is difficult and only the average surface energy for polycrystalline is available. Referring to previous works [23,28,29], we optimized the lowest surface energy ($E_{(110)}$) to approach the average value. Besides, in order to make the results comparable, the same experimental data as 1NN MEAM and 2NN MEAM were taken as the optimization targets in LI-MEAM, which were reported in Ref. [49–53].

Particle Swarm optimization (PSO) algorithm [32,33,54] was used to determine all the six parameters simultaneously. The six parameters, A, $\beta^{(0)}$, $t^{(1)}$, $t^{(2)}$, $t^{(3)}$ and r_c, were first given a set of initial values to start PSO algorithm. The five selected physical properties as fitting targets, C_{11}, C_{44}, $\Delta E_{bcc\to fcc}$, E_v^f, $E_{(110)}$, were calculated using this group of parameters based on LI-MEAM and the relative errors for each properties were calculated. A new group of parameters would be generated by PSO algorithm until the errors were acceptable. In order to guarantee the accuracy of some specified properties, different weighting factors were assigned to the calculated errors of different properties. Besides, we imposed reasonable parameter bounds to ensure the physical correctness of the model.

The final determined parameters of bcc-Fe based on LI-MEAM potential are listed in Table 1, compared with those obtained based on 1NN MEAM and 2NN MEAM. In the table, the former six parameters, E_c, r_e, B, $\beta^{(1)}$, $\beta^{(2)}$, $\beta^{(3)}$, were fixed on experimental or specified values during the optimization, the middle six parameters, A, $\beta^{(0)}$, $t^{(1)}$, $t^{(2)}$, $t^{(3)}$, r_c, were optimized, and the latter two, $C_{\max}$, $C_{\min}$, only existed in previous MEAM models. From Table 1, the cutoff distance, r_c, of bcc-Fe was optimized to be 5.678 Å based on LI-MEAM, which lies between the fifth and the sixth nearest neighbors of the equilibrium structure of bcc-Fe, and means that the interactions up to fifth nearest neighbor are considered. To illustrate the contributions of each order of nearest neighbors to the total pair energy, Fig. 2 was drawn. In the figure, the pair potential curve was given. The black bars show the ratios for the five different orders of nearest neighbors. The positions of the bars correspond to the m-th nearest neighbor distances. The deep valley of the pair potential curve corresponds to the first and second nearest neighbors, which means the pair interactions are relatively strong. Quantitatively, the pair energy from the first and second nearest neighbors donates about 83.6% of the total pair energy. For farther nearest neighbor contributions, even though the magnitudes of the pair potentials from third and fourth neighbors are tiny from the curve, the larger number of neighbors is much larger than those of first or second neighbors (12 for the third and 24 for the fourth). It is shown that the interactions from the third and fourth nearest neighbors donate up to 15.0% to the total energy, which could be significant in modeling some long range effect and have been previously neglected in other MEAM models. The fifth nearest neighbors contributes about 1.4% to the cohesive energy, which comes out as a reasonable a optimization result.

Fig. 3 shows the pair energies and embedding energies of bcc-Fe as a function of atom separation for 1NN MEAM, 2NN MEAM and LI-MEAM. The inset of Fig. 3(a) schematically shows how the cutoff distances map to the nearest neighbors for different models. As the figure shown, by taking increasing number of nearest neighbors into account from 1NN MEAM to 2NN MEAM and finally LI-MEAM, these curves become weaker with longer interaction ranges. Thus, LI-MEAM can approach a more realized physical picture since the contribution of interaction decays off gradually going to farther nearest neighbors.

3.2. Calculation of physical properties

The optimized potential parameters of bcc-Fe through the above procedures were used to compute some critical physical properties in order to evaluate the reliability of the developed LI-MEAM, such as formation energies of surface (100) and (111), $E_{(100)}$ and $E_{(111)}$, structure energy differences, $\Delta E_{fcc\to hcp}$, $\Delta E_{bcc\to sc}$, $\Delta E_{bcc\to dia}$, relative changes in nearest neighbor distance, $\Delta R_{bcc\to sc}$, $\Delta R_{bcc\to dia}$, vacancy migration energy barrier, E_v^m, and some thermal properties (thermal expansion coefficient, ε, specific heat, C_p, bulk melting point, T_{bm}). The experimental data and results calculated based on other potential models, EAM [23], 1NN MEAM, 2NN MEAM, are also presented in Table 2 as comparison. In the table, the properties above the middle horizontal line were used for the optimization of the potential parameters, while the others were predicted based on individual potential models. As illustrated in Table 2, all the properties used as the fitting targets could be reproduced accurately except $\Delta E_{bcc\to fcc}$, which is somewhat smaller than the experimental

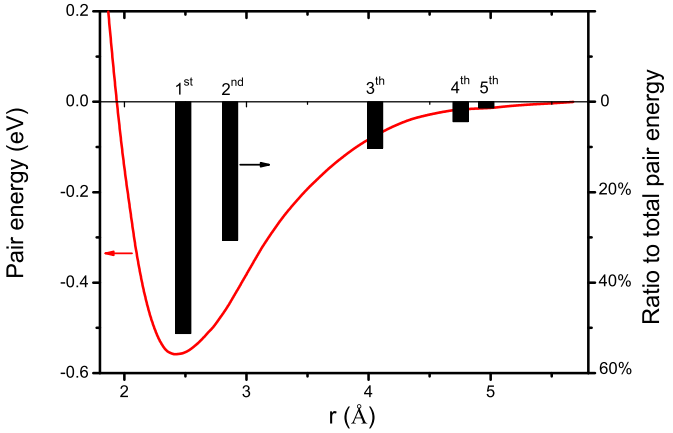

Fig. 2. The pair potential curve (red-solid curve) and the ratio of the pair energy (black bars) contributed by each order of nearest neighbors to the total pair energy of bcc-Fe based on LI-MEAM using the optimized parameters. (For interpretation of the references to colour in this figure legend, the reader is referred to the web version of this article.)

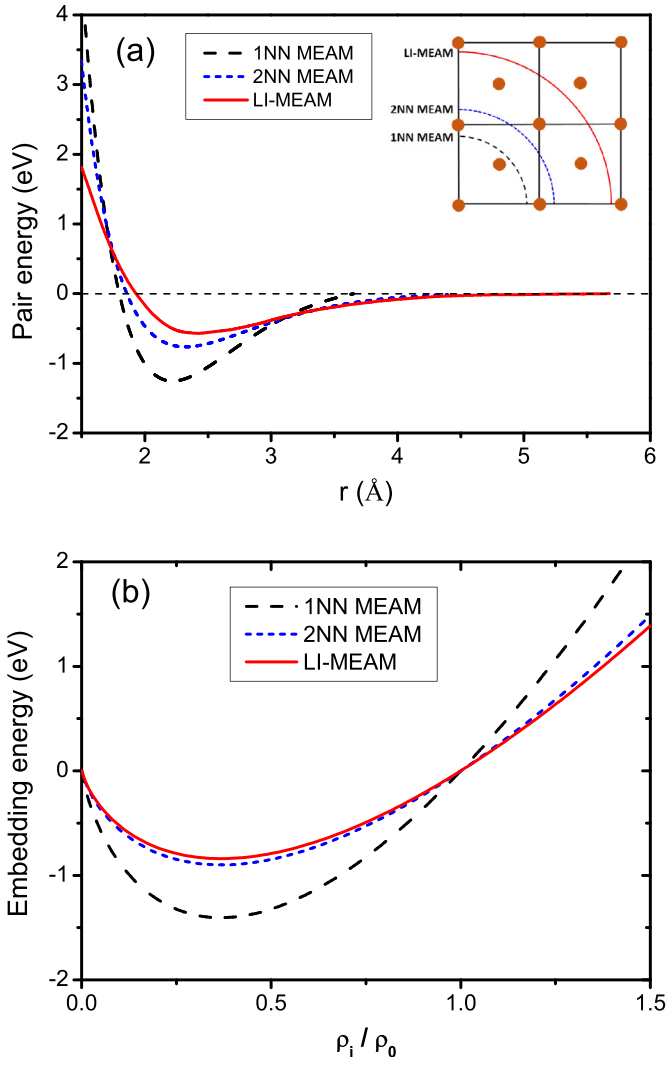

Fig. 3. Comparison of the pair energies (a) and the embedding energies (b) of bcc-Fe for different MEAM models (1NN MEAM, 2NN MEAM, LI-MEAM) using individual optimized parameters. The inset in figure (a) is a schematic diagram to illustrate how the cutoff distances map to the nearest neighbors for different MEAM models.

value and is near to that of 1NN MEAM and 2NN MEAM. Lee et al. [28] mentioned that one main problem of 1NN MEAM is its wrong prediction for the order of the surface energies among the three low-index surfaces. The experimental results have shown that the relationship of surface energy among surface (100), (110) and (111) is $E_{(110)} < E_{(100)} < E_{(111)}$ [55,56]. In present work, only the lowest surface energy [that of (110) surface] was selected as the fitting target and the other two surface energies were predicted with no constraint among them. The results shows that the order among the three low-index surface energies is in agreement with experimental data. Another problem of 1NN MEAM is its failure in the prediction of the ground structure for some bcc metals [28], such as bcc-Fe. Maintaining the right ground structure is a crucial test for specific interatomic potentials. The structural energy differences and relative changes in nearest neighbor distance between various crystal structures (bcc, fcc, sc and diamond) are also presented in Table 2. Among these items, $\Delta E_{bcc\to fcc}$ was used for fitting, $\Delta E_{fcc\to hcp}$, $\Delta E_{bcc\to sc}$, $\Delta E_{bcc\to dia}$, $\Delta R_{bcc\to sc}$ and $\Delta R_{bcc\to dia}$ were predicted. Here, the calculation on the hcp structure was done for a fixed ideal value of c/a, 1.633. The results show that LI-MEAM can give right ground structure. No experimental data is available for

Table 2
Calculated physical properties of bcc-Fe using the optimized parameters based on LI-MEAM, in comparison with experimental data and the previous calculations based on EAM (Ref. [23]), 1NN MEAM (Ref. [26]) and 2NN MEAM (Ref. [28]). Values listed are the elastic constants C_{11}, C_{12}, C_{44} (10^{12} dyn/cm^2), structure energy differences ΔE (eV/atom), relative changes in nearest neighbor distance ΔR (Å), vacancy formation energy E_v^f (eV), vacancy migration energy barrier E_v^m (eV), (100), (110), and (111) surface energy $E_{(100)}$, $E_{(110)}$, and $E_{(111)}$ (erg/cm^2), thermal expansion coefficient ε (10^{-6}/K), specific heat C_p (J/mol K) and melting point T_{bm} (K). The experimental elastic constants, structure energy differences, vacancy formation energy and migration energy barrier, surface energy and thermal properties are from Ref. [49], Ref. [50], Ref. [51], Ref. [52] and Ref. [53], respectively.

	Expt.	EAM	1NN MEAM	2NN MEAM	LI-MEAM
C_{11}	2.30	1.908	2.31	2.30	2.30
C_{12}	1.35	1.545	1.36	1.36	1.36
C_{44}	1.17	1.367	1.17	1.17	1.17
$\Delta E_{bcc\to fcc}$	0.082	0.082	0.03	0.041	0.044
E_v^f	1.79	2.29	1.55	1.67	1.79
$E_{(110)}$	2360	1946[a]	1634	2362	2427[a]
$E_{(100)}$		2060[a]	2406	2508	2547[a]
$E_{(111)}$		2308[a]	1768	2669	2771[a]
$\Delta E_{fcc\to hcp}$	−0.023	−0.029	−0.013	−0.014	−0.011
$\Delta E_{bcc\to sc}$		0.65	0.21	0.95	0.47
$\Delta R_{bcc\to sc}$				−0.10	−0.16
$\Delta E_{bcc\to dia}$			0.48	1.77	1.475
$\Delta R_{bcc\to dia}$				−0.26	−0.22
E_v^m	0.55	0.40			0.41
ε	12.1			11.0	11.3
C_p	25.5			26.0	24.1
T_{bm}	1811	1990		2020[b]	1872

[a] Unrelaxed values.
[b] The lower limit of the range in Ref. [28].

$\Delta E_{bcc\to sc}$, $\Delta E_{bcc\to dia}$, $\Delta R_{bcc\to sc}$ and $\Delta R_{bcc\to dia}$. However, the values calculated by 2NN MEAM and LI-MEAM are with very similar levels. The vacancy migration energy barrier, E_v^m, can also be predicted with acceptable accuracy based on LI-MEAM. Finally, some thermal properties, as thermal expansion coefficient, ε, specific heat, C_p, and bulk melting point, T_{bm}, were calculated. In order to make the results comparable with available results, the temperature regions were controlled between 100 K and 400 K for the calculations of ε and C_p. As to the calculation of T_{bm}, REMD method was used. From the calculated results shown in Table 2, it can be found that the thermal expansion coefficient and the specific heat are in agreement with the experimental results. Especially, the bulk melting point, which is commonly overestimated, was predicted with excellent accuracy.

From the perspective of reproducing the fitting targets and predicting the basic physical properties, LI-MEAM shows comparable performance and accuracy compared with all the other potential models. This shows the validity and reliability of LI-MEAM.

3.3. REMD simulations of NPs

To verify the transferability of the developed LI-MEAM, we further calculated melting of NPs aside from bulk properties of bcc-Fe. Herein, we employed 2NN MEAM and LI-MEAM potentials to carry out REMD simulations on a series of spherical bcc-Fe NPs (listed in Table 3) to study how the melting point depends on the size and further explore the melting mechanism of bcc-Fe NPs. Fig. 4(a) gives the calculated melting curves, which are expressed as the changing of potential energy per atom with respect to the temperature, for different diameters of bcc-Fe NPs based on LI-MEAM. Besides, three snapshots of cross section of D70-NP at different temperatures (0 K, 1680 K, 1700 K), visualized by AtomEye [57], are shown in Fig. 4(b). The coloring denotes the coordination number. The initial structure of D70-NP at 0 K is very regular and all the inner atoms appear to be MistyRose, which means their

Table 3
Detailed information of each spherical bcc-Fe NP used in present work, and the corresponding melting point (K) calculated based on 2NN MEAM and LI-MEAM. *D* (Å) and *N* are the diameter and number of atoms, respectively.

System	*D*	*N*	Melting point	
			2NN MEAM	LI-MEAM
D25	25	725	1228	1145
D30	30	1243	1438	1309
D35	35	1924	1574	1431
D40	40	2874	1662	1508
D45	45	4088	1709	1565
D50	50	5601	1745	1603
D55	55	7391	1797	1635
D60	60	9640	1815	1658
D65	65	12278	1823	1681
D70	70	15353	1857	1700
D80	80	22899	1877	1720

coordination numbers are 14. When the temperature increases to 1680 K, some atoms appear in the inner of D70-NP (RoyalBlue or Cyan atoms in the small circle), which means the number of their nearest neighbors increases or decreases by one. Even so, these atoms are still near their initial positions. Hence, the changing of coordination numbers mainly results from the intense thermal vibration. However, the surface irregular atoms increases to two or three layers (in the annulus zone), which could be regarded as evidence of surface melting. When the temperature continually reaches 1700 K, a sharp increase of the potential energy per atom appears, and the corresponding structure of D70-NP is totally a mass, not only for the coordination number, but also for the structure. The NP at 1700 K could be regarded as a totally melted one and the corresponding temperature could be defined as the melting point.

Using the same definition, the melting points of all the NPs based on 2NN MEAM and LI-MEAM can be obtained, which are listed in Table 3. Meanwhile, these melting points are drawn in Fig. 5(a) as a function of the diameter of NPs. The corresponding melting points of bulk bcc-Fe are also plotted as horizontal lines. One common feature is that the melting points of NPs are lower than that of corresponding bulk material with the minimum gap being about 150 K for both potential models. Besides, from the tendency of the melting curves of NPs, it is reasonable to surmise that the melting point of NPs should be approaching to that of bulk

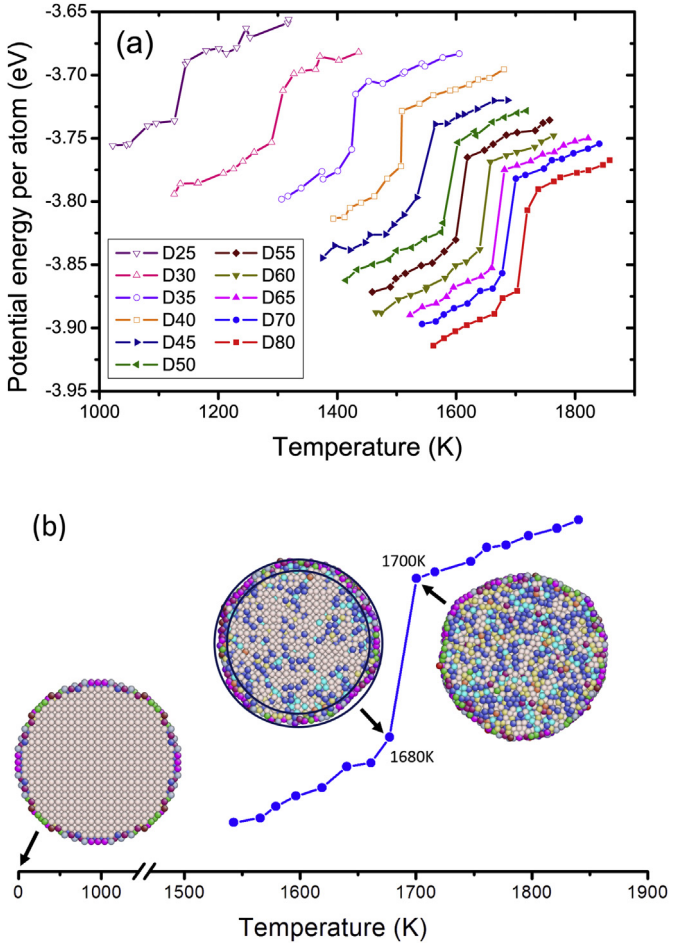

Fig. 4. (a) Calculated melting curves of different sizes of spherical bcc-Fe NPs using REMD simulations based on LI-MEAM using the optimized parameters. (b) Snapshots of cross section of D70-NP at three different temperatures (0 K, 1680 K, 1700 K) during heating. Coloring denotes the coordination number. (Main colors with respect to the coordination numbers: Gray, 4; Red, 5; RoyalBlue, 13; MistyRose, 14; Cyan, 15; Coral, 16; Green, 17). (For interpretation of the references to colour in this figure legend, the reader is referred to the web version of this article.)

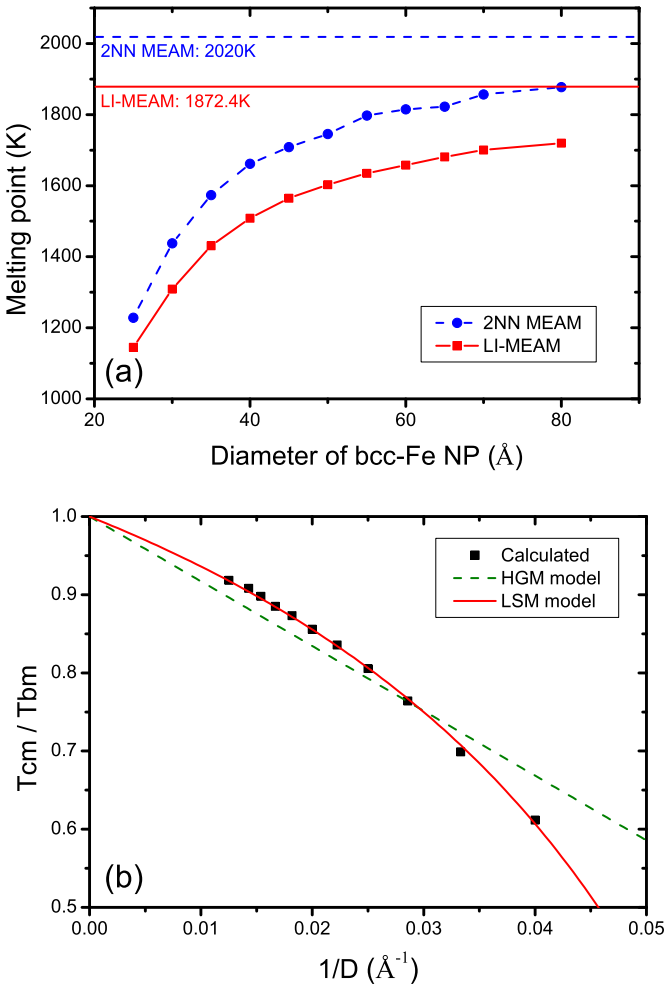

Fig. 5. (a) Melting point of bcc-Fe NP as a function of the diameter calculated using 2NN MEAM (blue-dash) and LI-MEAM (red-solid). The horizontal lines represent the melting points of corresponding bulk materials. (b) The reduced melting temperature as a function of the inverse diameter of bcc-Fe NP based on LI-MEAM. The black squares are the REMD calculated results, and the dash-green and solid-red curves represent the fitted results using HGM and LSM models, respectively. (For interpretation of the references to colour in this figure legend, the reader is referred to the web version of this article.)

for extremely larger NPs. On the other hand, referring to the experimental value of the melting point of bulk bcc-Fe (1811K), 2NN MEAM overestimates the melting points of both the bulk and the NPs of bcc-Fe, while LI-MEAM could give more reasonable results. In addition, the curve based on LI-MEAM is slightly smoother than that of 2NN MEAM. We attribute it to the larger cutoff distance LI-MEAM used, which generally leads to less abrupt changes in MD simulations and thus a smoother curve. In order to explore the melting mechanism of spherical bcc-Fe NPs, we have compared the calculated relationship between T_{cm}/T_{bm} and $1/D$ with the LSM and HSM model in Fig. 5(b). In the figure, the black squares represent the reduced melting temperature as the function of the inverse diameter of NP, the dash-green line and the solid-red curve represent the fitting results of HGM model and LSM model using Eqs. (24) and (25), respectively. It is obvious that LSM model could be better fitted to the REMD simulation results than HGM model, which means that the size-dependent melting behavior of bcc-Fe NPs is submitted to LSM model, rather than HGM model. This is in accordance with previous report [35]. Meanwhile, the constant thickness, δ, of the outer liquid shell in LSM model was fitted to be 5.22 $\AA$, which corresponds to two or three layers of atoms. This is consistent with the observation from Fig. 4(b), and confirms the pre-melting of the surface before the melting of the entire NP. The results confirm the availability and accuracy of LI-MEAM in modeling NP systems.

4. Conclusions

In present work, we developed a reliable procedure to simplify the MEAM interatomic potentials based on Chen-Möbius lattice inversion method. The many-body screening functions were removed and the interactions from farther nearest neighbors were considered. To validate LI-MEAM model, we optimized the potential parameters of bcc-Fe and calculated its physical properties, which agree well with experimental values. Finally, LI-MEAM was used to investigate the melting behavior of different sizes of bcc-Fe NPs by REMD simulations. It's found that the melting mechanism of bcc-Fe is subject to LSM model. Overall, LI-MEAM exhibits several advantages such as fewer parameters, more accurate melting points and smoother melting curves, on the calculations of physical properties.

Acknowledgments

The authors gratefully thank Prof. Nanxian Chen, Prof. Jiang Shen for helpful discussions about Chen-Möbius lattice inversion. This work is supported by the National Basic Research Program of China (2011CB606401 and 2013CB934800), National Natural Science Foundation of China (51101064 and 51302094) and Research Funds by State Key Laboratory of Material Processing and Die & Mould Technology, Huazhong University of Science and Technology. We thank the technology support by the Texas Advanced Computing Center (TACC) at the University of Texas at Austin (http://www.tacc.utexas.edu) for providing grid resources that have contributed to the research results reported within this paper.

References

[1] F.F. Abraham, R. Walkup, H. Gao, M. Duchaineau, T.D.D.L. Rubia, M. Seager, Simulating materials failure by using up to one billion atoms and the world's fastest computer: Brittle fracture, Proc. Nat. Acad. Sci. U S A 99 (2002) 5777.
[2] D.E. Shaw, P. Maragakis, K. Lindorff-Larsen, S. Piana, R.O. Dror, M.P. Eastwood, J.A. Bank, J.M. Jumper, J.K. Salmon, Y. Shan, W. Wriggers, Atomic-level characterization of the structural dynamics of proteins, Science 330 (2010) 341.
[3] J.H. Li, X.D. Dai, S.H. Liang, K.P. Tai, Y. Kong, B.X. Liu, Interatomic potentials of the binary transition metal systems and some applications in materials physics, Phys. Rep. 455 (2008) 1.
[4] M.S. Daw, M.I. Baskes, Semiempirical, quantum mechanical calculation of hydrogen embrittlement in metals, Phys. Rev. Lett. 50 (1983) 1285.
[5] M.S. Daw, M.I. Baskes, Embedded-atom method: derivation and application to impurities, surfaces, and other defects in metals, Phys. Rev. B 29 (1984) 6443.
[6] M.W. Finnis, J.E. Sinclair, A simple empirical N-body potential for transition metals, Philos. Mag. A 50 (1984) 45.
[7] F.H. Stillinger, T.A. Weber, Computer simulation of local order in condensed phases of silicon, Phys. Rev. B 31 (1985) 5262.
[8] J. Tersoff, New empirical approach for the structure and energy of covalent systems, Phys. Rev. B 37 (1988) 6991.
[9] R.A. Johnson, Analytic nearest-neighbor model for fcc metals, Phys. Rev. B 37 (1988) 3924.
[10] R.A. Johnson, D.J. Oh, Analytic embedded atom method model for bcc metals, J. Mater. Res. 4 (1989) 1195.
[11] Y.F. Ouyang, B.W. Zhang, S.Z. Liao, Z.P. Jin, A simple analytical EAM model for bcc metals including Cr and its application, Z. Phys. B 101 (1996) 161.
[12] W.Y. Hu, B.W. Zhang, B.Y. Huang, F. Gao, D.J. Bacon, Analytic modified embedded atom potentials for HCP metals, J. Phys. Condens. Matter 13 (2001) 1193.
[13] B. Lee, K. Cho, Extended embedded-atom method for platinum nanoparticles, Surf. Sci. 600 (2006) 1982.
[14] B. Shan, L. Wang, S. Yang, J. Hyun, N. Kapur, Y. Zhao, J.B. Nicholas, K. Cho, First-principles-based embedded atom method for PdAu nanoparticles, Phys. Rev. B 80 (2009) 035404.
[15] N.X. Chen, Modified möbius inverse formula and its applications in physics, Phys. Rev. Lett. 64 (1990) 1193.
[16] M. Li, N.X. Chen, Recovery of an N-body potential from a universal cohesion equation, Phys. Rev. B 52 (1995) 997.
[17] N.X. Chen, Z.D. Chen, Y.C. Wei, Multidimensional inverse lattice problem and a uniformly sampled arithmetic Fourier transform, Phys. Rev. E 55 (1997) 5.
[18] S. Zhang, N. Chen, Ab initio interionic potentials for NaCl by multiple lattice inversion, Phys. Rev. B 66 (2002) 064106.
[19] Y. Long, N.X. Chen, W.Q. Zhang, Pair potentials for a metal ceramic interface by inversion of adhesive energy, J. Phys. Condens. Matter 17 (2005) 2045.
[20] Q. Xie, M.C. Huang, Application of lattice inversion method to embedded-atom method, Phys. Status Solidi B 186 (1994) 393.
[21] Q. Xie, M.C. Huang, A lattice inversion method to construct the alloy pair potential for the embedded-atom method, J. Phys. Condens. Matter 6 (1994) 11015.
[22] Q. Xie, N.X. Chen, Recovery of an N-body potential from a universal cohesion equation, Phys. Rev. B 51 (1995) 15856.
[23] X.-Y. Yuan, N.-X. Chen, J. Shen, W. Hu, Embedded-atom-method interatomic potentials from lattice inversion, J. Phys. Condens. Matter 22 (2010) 375503.
[24] M.I. Baskes, Application of the embedded-atom method to covalent materials: a semi empirical potential for silicon, Phys. Rev. Lett. 59 (1987) 2666.
[25] M.I. Baskes, J.S. Nelson, A.F. Wright, Semiempirical modified embedded-atom potentials for silicon and germanium, Phys. Rev. B 40 (1989) 6085.
[26] M.I. Baskes, Modified embedded-atom potentials for cubic materials and impurities, Phys. Rev. B 46 (1992) 2727.
[27] M.I. Baskes, Atomistic potentials for the molybdenum silicon system, Mater. Chem. Phys. 50 (1997) 152.
[28] B.-J. Lee, M.I. Baskes, Second nearest-neighbor modified embedded-atom-method potential, Phys. Rev. B 62 (2000) 8564.
[29] B.-J. Lee, M.I. Baskes, Second nearest-neighbor modified embedded atom method potentials for bcc transition metals, Phys. Rev. B 64 (2001) 184102.
[30] B.-J. Lee, J.-H. Shim, M.I. Baskes, Semiempirical atomic potentials for the fcc metals Cu, Ag, Au, Ni, Pd, Pt, Al, and Pb based on first and second nearest-neighbor modified embedded atom method, Phys. Rev. B 68 (2003) 144112.
[31] B.-J. Lee, B.D. Wirth, J.-H. Shim, J. Kwon, S.C. Kwon, J.-H. Hong, Modified embedded-atom method interatomic potential for the Fe-Cu alloy system and cascade simulations on pure Fe and Fe-Cu alloys, Phys. Rev. B 71 (2005) 184205.
[32] Z.W. Cui, F. Gao, Z.H. Cui, J.M. Qu, Developing a second nearest-neighbor modified embedded atom method interatomic potential for lithium, Modell. Simul. Mater. Sci. Eng 20 (2012) 15014.
[33] Z.W. Cui, F. Gao, Z.H. Cui, J.M. Qu, A second nearest-neighbor embedded atom method interatomic potential for LiCSi alloys, J. Power Sources 207 (2012) 150.
[34] Y. Sugita, Y. Okamoto, Replica-exchange molecular dynamics method for protein folding, Chem. Phys. Lett. 314 (1999) 141.
[35] Q. Shu, Y. Yang, Y. Zhai, D.Y. Sun, H.J. Xiang, X.G. Gong, Size-dependent melting behavior of iron nanoparticles by replica exchange molecular dynamics, Nanoscale 4 (2012) 6307.
[36] N.X. Chen, C.F. Zhang, M. Zhou, G.B. Ren, W.B. Zhao, Closed-form solution for inverse problems of Fermi systems, Phys. Rev. E 48 (1993) 1558.
[37] Q. Xie, N.X. Chen, Unified inversion technique for fermion and boson integral equations, Phys. Rev. E 52 (1995) 351.
[38] N.X. Chen, E.Q. Rong, Unified solution of the inverse capacity problem, Phys. Rev. E 57 (1998) 1302.
[39] J.H. Rose, J.R. Smith, F. Guinea, J. Ferrante, Universal features of the equation of state of metals, Phys. Rev. B 29 (1984) 2963.

[40] L. Wu, Y. Zhang, Y. Wen, Z. Zhu, S. Sun, Molecular dynamics investigation of structural evolution of fcc Fe nanoparticles under heating process, Chem. Phys. Lett. 502 (2011) 207.
[41] Y. Shibuta, T. Suzuki, Melting and solidification point of fcc-metal nanoparticles with respect to particle size: a molecular dynamics study, Chem. Phys. Lett. 498 (2010) 323.
[42] S.H. Mahboobi, A. Meghdari, N. Jalili, F. Amiri, Qualitative study of nanocluster positioning process: planar molecular dynamics simulations, Curr. Appl. Phys. 9 (2009) 997.
[43] Q. Jiang, S. Zhang, M. Zhao, Size-dependent melting point of noble metals, Mater. Chem. Phys. 82 (2003) 225.
[44] K.K. Nanda, Size-dependent melting of nanoparticles: hundred years of thermodynamic model, Pramana 72 (2009) 617.
[45] W.H. Qi, M.P. Wang, Size and shape dependent melting temperature of metallic nanoparticles, Mater. Chem. Phys. 88 (2004) 280.
[46] M. Attarian Shandiz, A. Safaei, S. Sanjabi, Z.H. Barber, Modeling size dependence of melting temperature of metallic nanoparticles, J. Phys. Chem. Solids 68 (2007) 1396.
[47] H. Duan, F. Ding, A. Rosén, A.R. Harutyunyan, S. Curtarolo, K. Bolton, Size dependent melting mechanisms of iron nanoclusters, Chem. Phys. 333 (2007) 57.
[48] S.J. Plimpton, Fast parallel algorithms for short-range molecular dynamics, J. Comput. Phys. 117 (1995) 1.
[49] Landolt-Börnstein, Numerical Data and Functional Relationships in Science and Technology, Springer-Verlag, Berlin, 1979.
[50] A. Fernández Guillermet, P. Gustafson, An assessment of the thermodynamic properties and the (p,T) phase diagram of iron, High. Temp. High Press 16 (1985) 591.
[51] M.L. Swanson, G.R. Piercy, G.V. Kidson, A.F. Quenneville, Defects in quenched zirconium, J. Nucl. Mater. 34 (1970) 340.
[52] W.R. Tyson, W.A. Miller, Surface free energies of solid metals: estimation from liquid surface tension measurements, Surf. Sci. 62 (1977) 267.
[53] H. Okamoto, Phase Diagrams of Binary Iron Alloys, ASM International, Ohio, 1993.
[54] J. Kennedy, R. Eberhart, Particle swarm optimization, IEEE Trans. Neural Netw. (1995) 1942.
[55] B.E. Sundquist, A direct determination of the anisotropy of the surface free energy of solid gold, silver, copper, nickel, and alpha and gamma iron, Acta Metall. 12 (1964) 67.
[56] H.E. Grenga, R. Kumar, Surface energy anisotropy of iron, Surf. Sci. 61 (1976) 283.
[57] J. Li, AtomEye: an effcient atomistic confguration viewer, Model. Simul. Mater. Sci. Eng 11 (2003) 173.